

Active Darcy’s Law

Ryan R. Keogh,¹ Timofey Kozhukhov,¹ Kristian Thijssen,² and Tyler N. Shendruk^{1,*}

¹*School of Physics and Astronomy, The University of Edinburgh, Peter Guthrie Tait Road, Edinburgh, EH9 3FD, United Kingdom*

²*Niels Bohr Institute, University of Copenhagen, Blegdamsvej 17, Copenhagen, Denmark.*

While bacterial swarms can exhibit active turbulence in vacant spaces, they naturally inhabit crowded environments. We numerically show that driving disorderly active fluids through porous media enhances Darcy’s law. While purely active flows average to zero flux, hybrid active/driven flows display greater drift than pure-driven fluids. This enhancement is non-monotonic with activity, leading to an optimal activity to maximise flow rate. We incorporate the active contribution into an active Darcy’s law, which may serve to help understand anomalous transport of swarming in porous media.

Active fluids spontaneously flow because energy is locally injected by inherently out-of-equilibrium particles [1], such as motile cells [2] and exhibit collective dynamics on scales many times larger than individual cells [3]. Such coherent flows—uncorrelated at large spatio-temporal scales—describe many cellular systems, including swarming bacteria [4–6] and disorderly bacterial turbulence [7–9]. These flows have been studied in engineered geometries, e.g. channels [10, 11], cavities [12–14], annuli [15, 16], connected voids [17], pillar arrays [18, 19], ratchets [20], slits [21] and periodic obstacles [22–26]. However, many naturally occurring examples of collective bacterial motion arise in heterogeneous environments, such as porous media [27–29].

Individual self-propelled particles in the vicinity of obstacles have been studied, including bacteria [30–33], active Brownian particles [34–36] and active polymers [37–39]. Heterogeneity can have profound effects, on individual and collective dynamics, including clogging [30, 40–42], rectified conductivity [43], boundary migration [44], intermittency [45], redistribution [46, 47], chemotactic response [48–50], topological flocking [51] and other novel collective movements [52–55]. Indeed, the generality of anomalous motion in heterogeneous media [56–60] suggests porosity crucially alters active collective transport [61].

Here, we study the cooperative effect of disorderly active flows on pressure-driven transport through porous materials of fixed obstacles (**Fig. 1a**). We find that, when biased due to weak external pressure gradients, activity positively enhances global drift, even in the active turbulence limit. This effect endures as the number density of obstacles is increased, resulting in undiminished kinetic energy despite increased dissipative drag—suggesting active flows autonomously fill the available porous length scales. The active auxiliary flux increases with pressure gradient and is non-monotonic with activity, possessing an optimal activity. We conclude that the flux of active fluids through porous media are described by a modified Darcy’s law.

While individual swimming bacteria move with polar self-propulsion, their dipolar hydrodynamic and head-tail-symmetric steric interactions are nematic, making active nematics an appropriate minimal model [62–64], in agreement with experiments [5, 9, 65, 66]. To model active nematic fluids within a complex geometry, we employ active-nematic

Multi-Particle Collision Dynamics (AN-MPCD [67]), a recent mesoscopic method [68]. AN-MPCD simulates linearised fluctuating nematodynamics with isotropic viscosity and elasticity [69], and activity ζ modelled via local multi-particle force dipoles [70]. The competition between elasticity and activity results in an active length scale ℓ_ζ (**Fig. S1**). The corresponding continuum equations correspond to low Reynolds number flows with linearised nematic elasticity and an active stress term [71, 72]. Systems of motile bacterial exhibit density fluctuations [14, 73], as does the particle-based AN-MPCD approach (**Fig. S2**), in contrast to continuum models that assume incompressibility. We focus on flow-aligning nematics with extensile activity ζ and a weak external forcing $-G = (\nabla P) \cdot \hat{x}$ due to a pressure gradient ∇P down the channel \hat{x} (**Fig. 1a**), which breaks the directional symmetry of bacterial turbulence [7]. Values are reported in MPCD units [67] and unless otherwise stated, $G = 0.011$ and $\zeta = 0.08 \ell_\zeta \approx 10$. All other parameters are chosen to match previous studies characterising the numerical approach [68]. AN-MPCD is ideal for simulating active flows around randomly-placed off-lattice obstacles with a broad distribution of voids. The active fluid and porous medium are confined within a 2D channel with height $h = 30$ and length $L = 150$ with impermeable, no-slip walls with free-nematic anchoring (**Fig. 1a**), which models well-defined experimental set-ups [57]. Finite-size effects (**Fig. S3**) and alternative anchoring conditions (**Fig. S4**) are considered in the supplementary materials. The porous medium is formed of impermeable, immobile, circular obstacles of radii $R = 2$ with the same boundary conditions as the walls, producing isotropic porosity $\phi \in [0.67, 1.0]$, where $\phi = 1.0$ is an empty channel and 0.67 is likely to be impermeable [67]. The random obstacles are homogeneously distributed (**Fig. 1a**) but overlaps are not permitted. Components of the velocity field $\mathbf{v} = v_x \hat{x} + v_y \hat{y}$ are averaged temporally t , longitudinally x and/or transversely y , denoted as $\langle \cdot \rangle_{x,y,t}$ to measure flow profiles and global fluxes.

Before considering cooperative effects, we quantify the properties of the porous medium. In the limit of zero activity and large porosity ($\phi \rightarrow 1$), the flow is relatively unobstructed and the mean velocity profile $\langle v_x \rangle_{x,t}(y)$ is parabolic (**Fig. 1b**; yellow). As the porosity is decreased, the greater number of obstacles slows the flow (**Fig. 1a**; middle $\phi = 0.87$) and broadens the profiles (**Fig. 1b**; pink). At low porosity, the effect of the walls is minimal compared to obstacle drag (**Fig. 1a**; bottom $\phi = 0.79$), producing plug-like flow (**Fig. 1b**; blue). The flow profiles follow the Brinkman equation [74]

* t.shendruk@ed.ac.uk

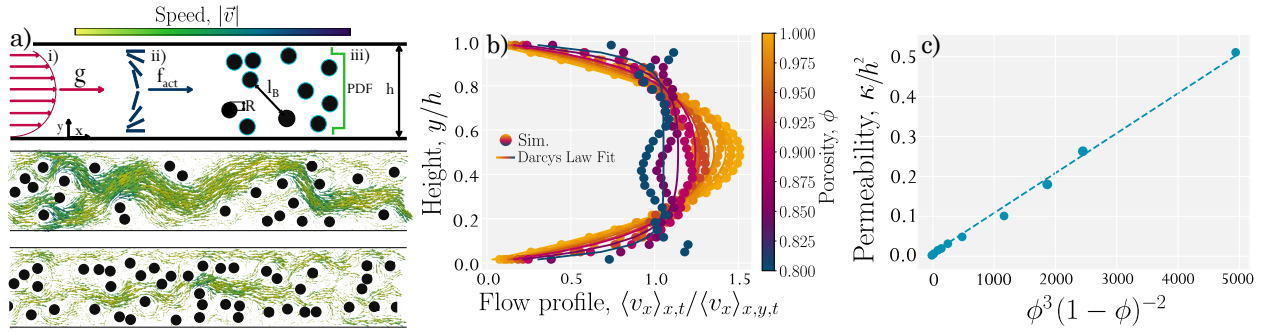


FIG. 1. **Purely pressure-driven flow through porous media.** **a)** Top: Schematic of pressure-driven active nematic fluids within a obstacle-laden rectangular channel of height h . *i)* Flow is driven by the pressure gradient $-G$. *ii)* Extensile active nematics generate local active forces \mathbf{f}_{act} . *iii)* Obstacles of radius R are placed with a homogeneous probability distribution function (PDF), without overlaps with each other or the walls, creating a porous medium characterised by Brinkman pore size ℓ_B . Middle: Snapshot of passive flow ($\zeta = 0$) due to a pressure gradient ($G = 0.011$) at porosity $\phi = 0.79$. The colour bar shows the magnitude of flow speed ranging from $0.0 \rightarrow 0.3$ in MPCD units. Bottom: Snapshots of passive flow ($\zeta = 0$) due to a pressure gradient ($G = 0.011$) at porosity $\phi = 0.87$. **b)** Normalised flow profiles $\langle v_x \rangle_{x,t}$ across the channel, fit by Eq. S(8) (solid lines). **c)** Permeability $\kappa = \ell_B^2$ from fits in (b) grow linearly with the Kozeny–Carman factor $\phi^3(1 - \phi)^{-2}$ (dashed line).

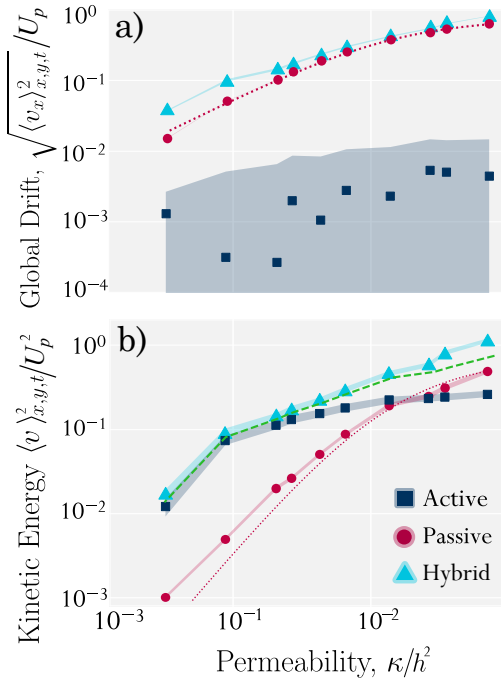


FIG. 2. **Global averaged flows.** \circ —Purely pressure-driven ($\zeta = 0$; $G = 0.011$), \square —Purely active ($\zeta = 0.08$ ($\ell_\zeta \simeq 10$); $G = 0$), and \triangle Hybrid active/pressure-driven ($\zeta = 0.08$; $G = 0.011$). Shaded regions denote standard error. **a)** Time averaged global drift $\langle v_x \rangle_{x,y,t}$ non-dimensionalised by Poiseuille flow U_p for $G = 0.011$. The pressure-driven case agrees with Darcy’s law (Eq. S(9)) ; dotted line), while the purely active case exhibits zero drift. **b)** Kinetic energy density $\langle v^2 \rangle_{x,y,t}$. Pressure-driven flow is consistent with theory (dotted red line) and hybrid flow coincides with the sum of the pure cases (dashed green line).

$[\partial_{yy} - \kappa^{-1}] \langle v_x \rangle_{x,t}(y) = -G/\eta$ for viscosity η and interstitial permeability κ [67], indicating that anisotropic properties can be absorbed into the Brinkman terms (Fig. 1b). At the lowest

porosity, systematic deviations, in the form of limited non-monotonic shoulders in the near-wall region appear (Fig. 1b; blue), due to steric inaccessibility of obstacles. From the fits, κ and corresponding pore size $\ell_B = \sqrt{\kappa}$ (or Brinkman length) are found (Fig. 1c). The resulting permeability obeys the Kozeny–Carman relationship $\kappa = c\phi^3(1 - \phi)^{-2}$ with $c = 0.091 \pm 0.004$.

As permeability κ decreases so does global drift $\langle v_x \rangle_{x,y,t}$ (Fig. 2a). In obstacle-laden channels ($\ell_B \ll h$), the drift is linearly dependent on κ , which follows from Darcy velocity $U_D \equiv G\kappa/\eta$ [67]; while in obstacle-free channels ($h \ll \ell_B$), the drift saturates to the expectation for Poiseuille flow $U_p \equiv Gh^2/12\eta$. Both are encompassed by $\langle v_x \rangle_{x,y,t} = U_D W(h/\ell_B)$, where the correction due to channel confinement $W(h/\ell_B) = 1 - (2\ell_B/h) \tanh(h/2\ell_B)$ depends only on the dimensionless ratio h/ℓ_B (Fig. 2a; dotted line [67]). Similarly, the kinetic energy density $\langle v^2 \rangle_{x,y,t} = U_D^2 [2 + \cosh(h/\ell_B) - (3\ell_B/h) \sinh(h/\ell_B)] / [1 + \cosh(h/\ell_B)]$ [67] is in good agreement with the simulations (Fig. 2b).

In contrast, purely active turbulent flows do not drift down the channel [7]. Even at lower activities, where spontaneous symmetry breaking results in unidirectional active flow, global drift averages to zero over multiple simulations [75]. We focus on activities which exhibit isotropic active turbulence in an obstacle-free channel ($h \gg \ell_B$) [76] (see movie 1). As $\phi \rightarrow 1$, the channel height h competes with the active length scale ℓ_ζ [77] to determine the spatiotemporal structure of the active flow [72, 75, 78, 79], which result in vortex lattices [72] recently observed as the first mode in suspensions of bacteria [11]. However, as obstacles are added, the confinement length switches from h to pore size ℓ_B . This causes the dynamics to transition from active turbulence to local unidirectional flows (Fig. 3a; top and movie 2). There are well defined paths in which unidirectional flow might arise, though spontaneous symmetry breaking might produce a stream of unidirectional flow moving in the opposite direction along other paths, or a recirculating vortex might become trapped in a void (Fig. 3a; top).

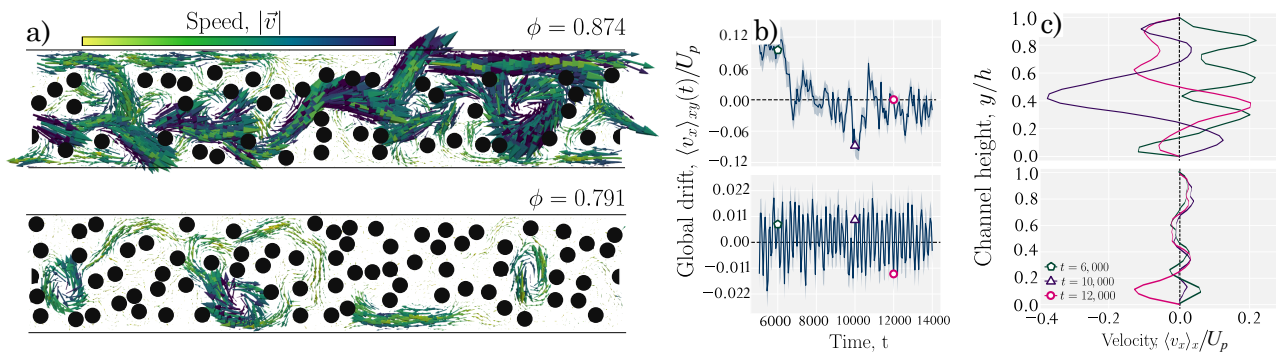


FIG. 3. **Purely active nematic** ($\zeta = 0.08$) **through porous media**. Top row: Porosity $\phi = 0.87$ ($\kappa/h^2 = 6.4 \times 10^{-3}$). Bottom row: $\phi = 0.79$ ($\kappa/h^2 = 2.3 \times 10^{-3}$). **a**) Snapshots of pressure-gradient-free ($G = 0$) active nematic flow. The colour bar represents the magnitude of flow speed in MPCD units from 0.0 \rightarrow 0.3. **b**) Instantaneous global drift $\langle v_x \rangle_{x,y}(t)$ non-dimensionalised by Poiseuille flow U_p for $G = 0.011$ for systems shown in (a). For the more dilute porous medium (top), the drift direction persists over time, whereas the denser system (bottom) exhibits more rapid fluctuations. Highlighted times: $\square - t = 6 \times 10^3$, $\triangle - 10 \times 10^2$, and $\circ - 12 \times 10^3$. **c**) Instantaneous flow profiles $\langle v_x \rangle_x(y; t)$ highlighted times in b).

The global drift $\langle v_x \rangle_{x,y}(t)$ quantifies the instantaneous new flux, and can persist for finite durations (**Fig. 3b**; top). Three instances illustrate different flow structures (**Fig. 3c**; top). First (**Fig. 3c**; top green), the instantaneous flow profile $\langle v_x \rangle_x(y, t)$ exhibits a significant net flux in the $+\hat{x}$ direction, despite opposing flow in the vicinity of the $y = 0$ wall. This net flux $\langle v_x \rangle_{x,y}(t)$ persists (**Fig. 3b**; top). The second moment (**Fig. 3c**; top purple) exhibits strong instantaneous flux $\langle v_x \rangle_{x,y}(t)$ in $-\hat{x}$ direction; however, it is short-lived (**Fig. 3b**; top). The third time (**Fig. 3c**; pink) illustrates that $\langle v_x \rangle_{x,y}(t)$ can be near-zero, despite non-zero flow in different regions of the channel.

While large porosity can allow otherwise turbulent active flows to instantaneously possess net global drift (**Fig. 3a**; top), lower porosity hinders instantaneous drift (**Fig. 3a**; bottom). In lower porosity, pore-entrapped vortices are more frequent and long-lived (**Fig. 3a**; bottom and **movie 3**). Furthermore, system-spanning streams are less likely and net fluxes become fleeting and noisier (**Fig. 3b**; bottom), while the instantaneous flow profiles $\langle v_x \rangle_x(y, t)$ approach zero across the channel (**Fig. 3c**; bottom). Although there are localised flows, drag on the obstacles generally dominates.

Ensemble averaged active drift is $\langle v_x \rangle_{x,y,t} = 0$, due to the spontaneous symmetry breaking in an absence of pressure gradients (**Fig. 2a**). However, despite zero net global flux in the purely active systems, there is significant global kinetic energy $\langle v^2 \rangle_{x,y,t}$ (**Fig. 2b**). Whereas kinetic energy drops rapidly with decreasing permeability κ for pressure-driven flows (**Fig. 2b**; red), active systems maintain higher kinetic energy at low permeability (**Fig. 2b**; blue). For $\zeta = 0.08$, the kinetic energy of the active flow is greater than the pressure-driven flow for $G = 0.011$ when $\kappa/h^2 \lesssim 0.11$. This is because active forces still generate locally coherent flow between obstacles and pores with sizes comparable to the active length scale ℓ_ζ trap vortices, allowing localised self-sustaining recirculations.

While purely active systems have zero flux, this is not true of hybridised flows that are both active and externally biased (**Fig. S5**). As in the purely activity case, activity ζ is chosen such that active flows are in the turbulent regime without

obstacles. The pressure gradient G is sufficiently high that activity acts as a perturbation to the driven case, but not so high that flow alignment is enforced. The kinetic energy density approximately corresponds to the sum of the two pure cases (**Fig. 2b**). At small pore sizes, the active kinetic energy of the hybrid system is close to that of the purely active flow. The hybrid flow begins to differ from the purely active case around $\kappa^*/h^2 \simeq 0.022$. Here, the ratio of the Brinkman length and active length scale is near unity ($\ell_B^*/\ell_\zeta \sim 4.5/10$).

The increased kinetic energy acts as an auxiliary driving force, assisting the pressure gradient to conduct fluid through the porous space. The global flux shows an augmented drift when compared to either the purely driven or purely active cases (**Fig. 2a**). Though the purely active flow is disorderly, in the hybrid case local active energy injection enhances the flux. To study the active contribution to the drift, we measure the difference $J = \langle v_x \rangle_{x,y,t}^H - \langle v_x \rangle_{x,y,t}^P$, where $\langle v_x \rangle_{x,y,t}^H$ is the global drift of the hybrid case and $\langle v_x \rangle_{x,y,t}^P$ is the purely pressure-driven case. We find $J > 0$ in all instances (**Fig. 4**), which reveals that even disorderly active flows enhance pressure-driven flux in porous systems. The active enhancement J increases linearly with κ at low permeability then saturates, going as $J(\kappa) \sim \kappa W(h/\sqrt{\kappa})$ (**Fig. 4a**). This is the same dependence as Darcy's law when going from a crowded channel to an obstacle-free channel (**Fig. 2**; red circles). Similarly at sufficiently small activity, the active contribution increases linearly with pressure gradient $J \sim G$ (**Fig. 4b**), suggesting the enhancement requires a coupling to the external biasing — the stronger the pressure gradient, the more the activity can boost the flux. Pressure gradients generate directed deformations to the orientation field \mathbf{Q} , which induce an auxiliary active forcing $f^{\text{act}} \sim \langle \partial_y^2 Q \rangle \sim G\zeta$ [80]. This approximation only holds in the limit $\dot{G} < \zeta/\ell_B$, since flow-alignment eventually suppresses divergence of Q and thus the active auxiliary forcing slows at larger pressure gradients. this approximation suggests the active contribution is linear with activity.

Indeed, varying activity ζ demonstrates that the enhancement $J(\zeta) \sim \zeta$ increases linearly at sufficiently low activities (**Fig. 4c**; **movie 4**). However, the auxiliary flux reaches

a maximum value at $\zeta^* = 0.05$ (**movie 5**), then decreases (**Fig. 4c**), indicating that there is an optimal activity for enhancing porous transport that is independent of the biasing pressure gradient. The maximum active contribution occurs when the ratio of the Brinkman and active length scales approach unity ($\ell_B/\ell_\zeta^* \sim 4.5/15$). For small activities (below the optimal value $\zeta < \zeta^*$), ℓ_ζ is larger than the characteristic pore size—disorderly active turbulence does not occur within the pores. Active flows are unidirectional and laminar-like within the pores; hence, $J \sim \zeta$. However for $\zeta > \zeta^*$, active turbulence is possible within the pores and collective flows become uncorrelated even on scales smaller than ℓ_B . The non-laminar uncorrelated turbulence generates additional kinetic dissipation and active vortices that are not conducive to flux (**movie 6**), causing the enhancement to decline as $J \sim \zeta^{-2}$ (**Fig. 4c**). In active nematics, much of the kinetic energy is contained with the vortices and so the additional dissipation scales with the change of enstrophy $f^{\text{disp}} \sim -\zeta^2$ [81].

Having obtained the active auxiliary contribution as a function of its dependencies, the full effect of local activity on the global flux is

$$J(\kappa, \zeta, G) = U_D \left[\frac{\zeta}{2\zeta^*} - \left(\frac{\zeta}{2\zeta^*} \right)^2 \right] W \left(\frac{h}{\ell_B} \right), \quad (1)$$

where $2\zeta^*$ is the optimal activity at which the active length scale ℓ_ζ matches the Brinkman length ℓ_B . The active contribution only depends directly on the Darcy velocity and dimensionless ratios. **Equation 1** is linear in pressure gradient for $G\ell_B/\zeta < 1$, nonlinear-but-monotonic with permeability and non-monotonic in activity, with a maximum where $\ell_\zeta = \ell_B$. The finite size of the channel enters through the factor of W [67]. The active contribution in **Eq. 1** is fit as a function of activity for a single pressure gradient (**Fig. 4c**; $G = 0.011$), with ζ^* the only fitting parameter since U_D and W are given by the permeability from **Fig. 1**. Having fit ζ^* for a single system, the predicted enhancement as a function of G and κ is seen to agree with all other simulations without any further fitting (**Fig. 4a-b**). The fit is accurate for activities above the pressure-dominated limit ($G\ell_B/\zeta > 1$), where and flow-alignment suppresses active forcing. Hence, activity enhances transport in porous channels via an effective active Darcy velocity

$$U_{\text{AD}} = \frac{G\kappa}{\eta} \left[1 + \frac{\zeta}{2\zeta^*} - \left(\frac{\zeta}{2\zeta^*} \right)^2 \right], \quad (2)$$

which recasts the Brinkman equation and channel-averaged drift into active Brinkman and drift equations by substitution of $U_D \rightarrow U_{\text{AD}}$. This prediction captures the enhancement of the flow profiles across the channel without additional fitting (**Fig. 4d**).

Here, we studied the auxiliary contribution of collective bacterial motion on fluid transport through porous media. Our results show that activity enhances transport of pressure-driven

fluids, even in the limit of bacterial turbulence. The pressure gradient breaks the symmetry of disorderly active flows, which enhances the total transport properties. Optimal activity for maximising the flux arises from competition between the characteristic active and porous length scales. By measuring the active contribution as a function of permeability, pressure gradient and activity, we discover an active version of Darcy's law. While the presented results are of active fluids and porous media confined within 2D channels, simulations of larger systems with periodic boundary conditions on all sides (**movies 7-8**) confirm the proposed active Darcy's law (**Fig. S6**). Through ζ^* , the active Darcy equation can be written as $U_{\text{AD}}/U_D = 1 + (\ell_B/\ell_\zeta)^2/2 - (\ell_B/\ell_\zeta)^4/4$.

This expands on recent work studying driven active fluids in empty channels [21, 80] and previous description of activity lowering the apparent viscosity [82–86] to complex disordered environments. While the active Darcy's law presented here could be interpreted as reducing the apparent viscosity, raising the effective permeability or augmenting the pressure gradient, none of these interpretations make clear the physical mechanism of weak pressure gradients biasing the local force densities $\sim \zeta/\ell_B$ within pores to point in the same direction, nor do they account for an optimal value for active auxiliary forcing when the active length scale is comparable to pore size.

The proposed active Darcy's law is particularly relevant for soil-associated bacteria as they collectively colonise plant roots within the rhizosphere [87]. Indeed, model organisms for active turbulence, including *Serratia marcescens* and *Bacillus subtilis*, are common rhizobacteria, with characteristic bacteria turbulence scales $\ell_\zeta \sim 30\mu\text{m}$ [6, 18, 66, 88–90]. These ℓ_ζ are comparable to characteristic pore sizes within rhizospheric soils with permeability $\kappa \sim 150\mu\text{m}^2$ [91] and $\ell_B \sim 20\mu\text{m}$ [92]. Our results indicate that $\ell_B/\ell_\zeta \sim 1$ is precisely the condition to maximise the active enhancement to the drift. Active transport enhancement could be utilised in future research as a framework to understand anomalous transport of nutrients by soil bacteria, as well as provide an approach for controlling active flows akin to continuous friction [93–95]. Previous work on dilute bacteria dynamics has highlighted the role of transient trapping [30, 52] and escape from cavities [96], and dead-end pores [97], and future work considering dense collective dynamics within random networks of cavities and dead-ends rather than obstacles may be fruitful. While we simulated immobile obstacles, future studies could consider how collective flows in turn modify deformable surroundings. Active clogging, erosion and infiltration may reveal much about the role of motile microbes as microecosystem engineers [98].

ACKNOWLEDGEMENTS

This research has received funding (T.N.S. and K.T.) from the European Research Council under the European Union's Horizon 2020 research and innovation programme (Grant Agreement Nos. 851196 and 101029079). For the purpose of open access, the author has applied a Creative Commons Attribution (CC BY) licence to any Author Accepted Manuscript version arising from this submission.

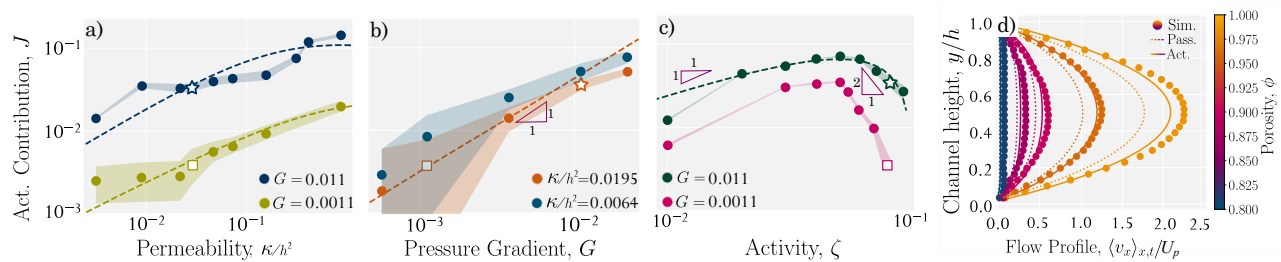


FIG. 4. **Active contribution J to hybridised flow.** \star and \blacksquare symbols denote the same data sets across panels, dashed lines represent fits, and shaded regions are the standard error. **a)** Dependence of J on permeability κ with $\zeta = 0.08$. Dashed lines predicted from **Eq. 1** with ζ^* fit of **Eq. 1** to the data in (c). **b)** Linear dependence of J on pressure gradient G for $\kappa/h^2 = 1.9 \times 10^{-2}$ and 6.4×10^{-3} with $\zeta = 0.08$. Dashed lines predicted from **Eq. 1** with ζ^* fit of **Eq. 1** to the data in (c). **c)** Non-monotonic dependence of J on ζ with a maximum at $\zeta^* = 0.05$ for $\kappa/h^2 = 1.9 \times 10^{-2}$ ($\phi = 0.93$) with $G = 0.011$ and 0.0011 . For $G = 0.011$, at low activity, $J \sim \zeta$, while $J \sim \zeta^{-2}$ at high activity. Fit of **Eq. 1** with $\zeta^* = 0.05 \pm 0.02$ shown as dashed yellow line. **d)** Hybrid flow profiles normalised by empty channel flow U_p compared with passive and active Darcy's laws. Simulated flow profiles (dots) for $G = 0.011$ compared to passive (dotted lines; **Eq. S(8)**) and active (solid lines; **Eq. 2**) Darcy's law predictions.

- [1] S. Shankar, A. Souslov, M. J. Bowick, M. C. Marchetti, and V. Vitelli, *Nature Reviews Physics* **4**, 380 (2022).
- [2] A. Be'er and G. Ariel, *Movement Ecology* **7**, 1 (2019).
- [3] R. Alert, J. Casademunt, and J.-F. Joanny, *Annual Review of Condensed Matter Physics* **13**, 143 (2022).
- [4] J. Nijjer, C. Li, Q. Zhang, H. Lu, S. Zhang, and J. Yan, *Nature Communications* **12**, 6632 (2021).
- [5] Z. Liu, W. Zeng, X. Ma, and X. Cheng, *Soft Matter* **17**, 10806 (2021).
- [6] I. S. Aranson, *Reports on Progress in Physics* **85**, 076601 (2022).
- [7] H. H. Wensink, J. Dunkel, S. Heidenreich, K. Drescher, R. E. Goldstein, H. Löwen, and J. M. Yeomans, *Proceedings of the National Academy of Sciences* **109**, 14308 (2012).
- [8] G. Ariel, M. Sidortsov, S. D. Ryan, S. Heidenreich, M. Bär, and A. Be'er, *Physical Review E* **98**, 032415 (2018).
- [9] Y. Peng, Z. Liu, and X. Cheng, *Science Advances* **7**, eabd1240 (2021).
- [10] S. P. Thampi, *Current Opinion in Colloid and Interface Science* **61**, 101613 (2022).
- [11] R. J. Henshaw, O. G. Martin, and J. S. Guasto, *Physical Review Fluids* **8**, 023101 (2023).
- [12] H. Wioland, F. G. Woodhouse, J. Dunkel, J. O. Kessler, and R. E. Goldstein, *Physical Review Letters* **110**, 268102 (2013).
- [13] E. Lushi, H. Wioland, and R. E. Goldstein, *Proceedings of the National Academy of Sciences* **111**, 9733 (2014).
- [14] S. Liu, S. Shankar, M. C. Marchetti, and Y. Wu, *Nature* **590**, 80 (2021).
- [15] H. Wioland, E. Lushi, and R. E. Goldstein, *New Journal of Physics* **18**, 075002 (2016).
- [16] A. Creppy, F. Plouraboué, O. Praud, X. Druart, S. Cazin, H. Yu, and P. Degond, *Journal of the Royal Society Interface* **13**, 20160575 (2016).
- [17] H. Wioland, F. G. Woodhouse, J. Dunkel, and R. E. Goldstein, *Nature Physics* **12**, 341 (2016).
- [18] D. Nishiguchi, I. S. Aranson, A. Snezhko, and A. Sokolov, *Nature Communications* **9**, 4486 (2018).
- [19] H. Reinken, D. Nishiguchi, S. Heidenreich, A. Sokolov, M. Bär, S. H. Klapp, and I. S. Aranson, *Communications Physics* **3**, 76 (2020).
- [20] R. Di Leonardo, L. Angelani, D. Dell'Arciprete, G. Ruocco, V. Iebba, S. Schippa, M. P. Conte, F. Mecarini, F. De Angelis, and E. Di Fabrizio, *Proceedings of the National Academy of Sciences* **107**, 9541 (2010).
- [21] F. Mackay, J. Toner, A. Morozov, and D. Marenduzzo, *Physical Review Letters* **124**, 187801 (2020).
- [22] P. Pietzonka, É. Fodor, C. Lohrmann, M. E. Cates, and U. Seifert, *Physical Review X* **9**, 041032 (2019).
- [23] H. Reinken, D. Nishiguchi, S. Heidenreich, A. Sokolov, M. Bär, S. H. Klapp, and I. S. Aranson, *Communications Physics* **3**, 76 (2020).
- [24] B. Zhang, B. Hilton, C. Short, A. Souslov, and A. Snezhko, *Physical Review Research* **2**, 043225 (2020).
- [25] C. Reichhardt and C. Reichhardt, *Physical Review E* **102**, 042616 (2020).
- [26] K. Chen and K. Qin, *Physics of Fluids* **34**, 023308 (2022).
- [27] M. Ranjbaran, M. Solhtalab, and A. K. Datta, *PLoS Computational Biology* **16**, e1007841 (2020).
- [28] Z. Wu, Y. Chen, D. Mukasa, O. S. Pak, and W. Gao, *Chemical Society Reviews* **49**, 8088 (2020).
- [29] M. Dentz, A. Creppy, C. Douarche, E. Clément, and H. Auradou, *Journal of Fluid Mechanics* **946**, A33 (2022).
- [30] T. Bhattacharjee and S. S. Datta, *Soft Matter* **15**, 9920 (2019).
- [31] V. R. Krishnamurthi, N. Harris, A. Rogers, M. Zou, and Y. Wang, *Colloids and Surfaces B: Biointerfaces* **209**, 112190 (2022).
- [32] M. Lee, C. Lohrmann, K. Szuttor, H. Auradou, and C. Holm, *Soft Matter* **17**, 893 (2021).
- [33] L. J. Perez, T. Bhattacharjee, S. S. Datta, R. Parashar, and N. L. Sund, *Physical Review E* **103**, 012611 (2021).
- [34] T. Jakuszeit, O. A. Croze, and S. Bell, *Physical Review E* **99**, 012610 (2019).
- [35] F. Moore, J. Russo, T. B. Liverpool, and C. P. Royall, *The Journal of Chemical Physics* **158**, 104907 (2023).
- [36] K. J. Modica, A. K. Omar, and S. C. Takatori, *Soft Matter* **19**, 1890 (2023).
- [37] Z. Mokhtari and A. Zippelius, *Physical Review Letters* **123**, 028001 (2019).
- [38] C. Kurzthaler, S. Mandal, T. Bhattacharjee, H. Löwen, S. S. Datta, and H. A. Stone, *Nature Communications* **12**, 7088 (2021).

- [39] L. Theeyancheri, S. Chaki, T. Bhattacharjee, and R. Chakrabarti, *Physical Review E* **106**, 014504 (2022).
- [40] K. Z. Coyte, H. Tabuteau, E. A. Gaffney, K. R. Foster, and W. M. Durham, *Proceedings of the National Academy of Sciences* **114**, E161 (2017).
- [41] D. Shrestha, J. Ou, A. Rogers, A. Jereb, D. Okyere, J. Chen, and Y. Wang, *Colloids and Surfaces B: Biointerfaces*, 113128 (2023).
- [42] A. Dehkharghani, N. Waisbord, and J. S. Guasto, *Communications Physics* **6**, 18 (2023).
- [43] N. Waisbord, A. Dehkharghani, and J. S. Guasto, *Nature Communications* **12**, 5949 (2021).
- [44] S. Rismani Yazdi, R. Nosrati, C. A. Stevens, D. Vogel, and C. Escobedo, *Biomicrofluidics* **12**, 011101 (2018).
- [45] E. Secchi, R. Rusconi, S. Buzzaccaro, M. M. Salek, S. Smriga, R. Piazza, and R. Stocker, *Journal of the Royal Society Interface* **13**, 20160175 (2016).
- [46] D. Scheidweiler, F. Miele, H. Peter, T. J. Battin, and P. de Anna, *Journal of the Royal Society Interface* **17**, 20200046 (2020).
- [47] T. W. Teo, X. Shen, and P. Y. Tan, *Microfluidics and Nanofluidics* **26**, 58 (2022).
- [48] T. Bhattacharjee, D. B. Amchin, J. A. Ott, F. Kratz, and S. S. Datta, *Biophysical Journal* **120**, 3483 (2021).
- [49] T. Bhattacharjee, D. B. Amchin, R. Alert, J. A. Ott, and S. S. Datta, *Elife* **11**, e71226 (2022).
- [50] B. Gao, X. Wang, and R. M. Ford, *Science of the Total Environment* **859**, 160004 (2023).
- [51] P. Rahmani, F. Peruani, and P. Romanczuk, *Communications Physics* **4**, 206 (2021).
- [52] T. Bhattacharjee and S. S. Datta, *Nature Communications* **10**, 2075 (2019).
- [53] I. Engelhardt, D. Patko, Y. Liu, M. Mimault, G. de Las Heras Martinez, T. George, M. MacDonald, M. Ptashnyk, T. Sukhodub, N. Stanley-Wall, *et al.*, *The ISME Journal* **16**, 2337 (2022).
- [54] D. B. Amchin, J. A. Ott, T. Bhattacharjee, and S. S. Datta, *PLoS Computational Biology* **18**, e1010063 (2022).
- [55] Y. Ben Dor, S. Ro, Y. Kafri, M. Kardar, and J. Tailleur, *Physical Review E* **105**, 044603 (2022).
- [56] K. Alim, S. Parsa, D. A. Weitz, and M. P. Brenner, *Physical Review Letters* **119**, 144501 (2017).
- [57] A. Anbari, H.-T. Chien, S. S. Datta, W. Deng, D. A. Weitz, and J. Fan, *Small* **14**, 1703575 (2018).
- [58] H. Wu and D. K. Schwartz, *Accounts of Chemical Research* **53**, 2130 (2020).
- [59] T. Shende, D. Mangal, J. C. Conrad, V. Niasar, and M. Babaei, *Physical Review E* **106**, 015103 (2022).
- [60] D. Fan, E. Chapman, A. Khan, F. Iacoviello, G. Mikutis, R. Pini, and A. Striolo, *Journal of Colloid and Interface Science* **617**, 94 (2022).
- [61] M. Kumar, J. S. Guasto, and A. M. Ardekani, *Journal of Rheology* **66**, 375 (2022).
- [62] A. Baskaran and M. C. Marchetti, *Physical Review Letters* **101**, 268101 (2008).
- [63] D. Saintillan and M. J. Shelley, *Complex Fluids in Biological Systems: Experiment, Theory, and Computation*, 319 (2015).
- [64] A. Peshkov, E. Bertin, F. Ginelli, and H. Chaté, *The European Physical Journal Special Topics* **223**, 1315 (2014).
- [65] D. Nishiguchi, K. H. Nagai, H. Chaté, and M. Sano, *Physical Review E* **95**, 020601 (2017).
- [66] H. Li, X. qing Shi, M. Huang, X. Chen, M. Xiao, C. Liu, H. Chaté, and H. P. Zhang, *Proceedings of the National Academy of Sciences* **116**, 777 (2019).
- [67] See Supplemental Material [url] for simulation details, derivations and additional numerical results, which includes Refs. [99–112].
- [68] T. Kozhukhov and T. N. Shendruk, *Science Advances* **8**, eabo5788 (2022).
- [69] H. Hfjar, *Condensed Matter Physics* **22**, 13601 (2019).
- [70] T. Kozhukhov, B. Loewe, and T. N. Shendruk, arXiv preprint arXiv:2401.17777 (2024).
- [71] A. Doostmohammadi, J. Ignés-Mullol, J. M. Yeomans, and F. Sagués, *Nature Communications* **9**, 3246 (2018).
- [72] T. N. Shendruk, A. Doostmohammadi, K. Thijssen, and J. M. Yeomans, *Soft Matter* **13**, 3853 (2017).
- [73] H. P. Zhang, A. Be'er, E.-L. Florin, and H. L. Swinney, *Proceedings of the National Academy of Sciences* **107**, 13626 (2010).
- [74] L. Durlofsky and J. Brady, *Physics of Fluids* **30**, 3329 (1987).
- [75] J. Hardoüin, R. Hughes, A. Doostmohammadi, J. Laurent, T. Lopez-Leon, J. M. Yeomans, J. Ignés-Mullol, and F. Sagués, *Communications Physics* **2**, 121 (2019).
- [76] A. Doostmohammadi, T. N. Shendruk, K. Thijssen, and J. M. Yeomans, *Nature Communications* **8**, 15326 (2017).
- [77] E. J. Hemingway, P. Mishra, M. C. Marchetti, and S. M. Fielding, *Soft Matter* **12**, 7943 (2016).
- [78] R. R. Keogh, S. Chandragiri, B. Loewe, T. Ala-Nissila, S. P. Thampi, and T. N. Shendruk, *Physical Review E* **106**, L012602 (2022).
- [79] L. C. Head, C. Dore, R. R. Keogh, L. Bonn, G. Negro, D. Marenduzzo, A. Doostmohammadi, K. Thijssen, T. Lopez-Leon, and T. N. Shendruk, *Nature Physics* (2024).
- [80] J. Walton, G. McKay, M. Grinfeld, and N. J. Mottram, *The European Physical Journal E* **43**, 1 (2020).
- [81] L. Giomi, *Physical Review X* **5**, 031003 (2015).
- [82] M. Cates, S. Fielding, D. Marenduzzo, E. Orlandini, and J. Yeomans, *Physical Review Letters* **101**, 068102 (2008).
- [83] L. Giomi, T. B. Liverpool, and M. C. Marchetti, *Physical Review E* **81**, 051908 (2010).
- [84] D. Saintillan, *Annual Review of Fluid Mechanics* **50**, 563 (2018).
- [85] A. Loisy, J. Eggers, and T. B. Liverpool, *Physical Review Letters* **121**, 018001 (2018).
- [86] V. A. Martinez, E. Clément, J. Arlt, C. Douarche, A. Dawson, J. Schwarz-Linek, A. K. Creppy, V. Škultéty, A. N. Morozov, H. Auradou, *et al.*, *Proceedings of the National Academy of Sciences* **117**, 2326 (2020).
- [87] A. Venieraki, P. Tsalgatidou, D. Georgakopoulos, M. Dimou, and P. Katinakis, *Hellenic Plant Protection Journal* **9**, 16 (2016).
- [88] A. Sokolov and I. S. Aranson, *Physical Review Letters* **109**, 248109 (2012).
- [89] A. Sokolov, I. S. Aranson, J. O. Kessler, and R. E. Goldstein, *Physical Review Letters* **98**, 158102 (2007).
- [90] R. Ran, D. A. Gagnon, A. Morozov, and P. E. Arratia, arXiv preprint arXiv:2111.00068 (2022).
- [91] N. Koebernick, K. R. Daly, S. D. Keyes, T. S. George, L. K. Brown, A. Raffan, L. J. Cooper, M. Naveed, A. G. Bengough, I. Sinclair, P. D. Hallett, and T. Roose, *New Phytologist* **216**, 124 (2017).
- [92] N. Koebernick, K. R. Daly, S. D. Keyes, A. G. Bengough, L. K. Brown, L. J. Cooper, T. S. George, P. D. Hallett, M. Naveed, A. Raffan, and T. Roose, *New Phytologist* **221**, 1878 (2019).
- [93] C.-M. Koch and M. Wilczek, *Physical Review Letters* **127**, 268005 (2021).
- [94] K. Thijssen, D. A. Khaladj, S. A. Aghvami, M. A. Gharbi, S. Fraden, J. M. Yeomans, L. S. Hirst, and T. N. Shendruk, *Proceedings of the National Academy of Sciences* **118**, e2106038118 (2021).

- [95] B. Martínez-Prat, R. Alert, F. Meng, J. Ignés-Mullol, J.-F. m. c. Joanny, J. Casademunt, R. Golestanian, and F. Sagués, *Physical Review X* **11**, 031065 (2021).
- [96] H. Wu, B. Greydanus, and D. K. Schwartz, *Proceedings of the National Academy of Sciences* **118**, e2101807118 (2021).
- [97] A. D. Bordoloi, D. Scheidweiler, M. Dentz, M. Bouabdellaoui, M. Abbarchi, and P. de Anna, *Nature Communications* **13**, 3820 (2022).
- [98] L. Brussaard, *Ambio* **26**, 563 (1997).
- [99] D. Saintillan and M. J. Shelley, *Comptes Rendus Physique* **14**, 497 (2013).
- [100] A. Malevanets and R. Kapral, *The Journal of Chemical Physics* **110**, 8605 (1999).
- [101] G. Gompper, T. Ihle, D. Kroll, and R. Winkler, *Advanced computer simulation approaches for soft matter sciences III*, 1 (2009).
- [102] H. Noguchi, N. Kikuchi, and G. Gompper, *EPL (Europhysics Letters)* **78**, 10005 (2007).
- [103] T. N. Shendruk and J. M. Yeomans, *Soft Matter* **11**, 5101 (2015).
- [104] S. P. Thampi, R. Golestanian, and J. M. Yeomans, *Physical Review Letters* **111**, 118101 (2013).
- [105] D. S. Bolintineanu, J. B. Lechman, S. J. Plimpton, and G. S. Grest, *Physical Review E* **86**, 066703 (2012).
- [106] M. L. Blow, M. Aqil, B. Liebchen, and D. Marenduzzo, *Soft Matter* **13**, 6137 (2017).
- [107] H. Liu, P. R. Patil, and U. Narusawa, *Entropy* **9**, 118 (2007).
- [108] J. G. Berryman and S. C. Blair, *Journal of Applied Physics* **62**, 2221 (1987).
- [109] R. F. Probstein, *Physicochemical Hydrodynamics* (John Wiley & Sons, Ltd, 1994).
- [110] K. M. Graczyk and M. Matyka, *Scientific Reports* **10**, 21488 (2020).
- [111] M. E. Cates and J. Tailleur, *Annual Review of Condensed Matter Physics* **6**, 219 (2015).
- [112] S. Ramaswamy, R. A. Simha, and J. Toner, *Europhysics Letters* **62**, 196 (2003).